Int. J. Heat Mass Transfer. Vol. 33, No. 1, pp. 139–149, 1990
Printed in Great Britain

0017-9310/90 $3.00 + 0.00

Simulation of pure metal melting with buoyancy and surface tension forces in the liquid phase

T. L. BERGMAN
Department of Mechanical Engineering, The University of Texas at Austin, Austin, TX 78712, U.S.A.

and

B. W. WEBB
Department of Mechanical Engineering, Brigham Young University, Provo, UT 84602, U.S.A.

(*Received* 13 *October* 1988 *and in final form* 9 *May* 1989)

Abstract—Analytical results are presented for the melting of a pure metal from an isothermal vertical wall. The investigation focuses on the influence of surface tension on the flow and heat transfer in the liquid phase as well as the resultant shape and motion of the solid–liquid interface. A control volume-based discretization scheme is used to solve the governing partial differential equations in the irregular melt domain while the moving boundary is immobilized by invoking the quasi-steady assumption. Numerical predictions reveal a complex interaction between buoyancy forces in the melt and the Marangoni effects at the melt free surface. The surface tension-driven convection causes isotherm compaction near the top of, and adjacent to the melting front. The associated high heat transfer at the intersection of the solid–liquid interface and the melt free surface results in significant 'notching' of the solid. Hence, the influence of Marangoni convection is felt strongly in the timewise shape and motion of the solid–liquid interface. Predicted global melting rates, however, exhibit less sensitivity to the inclusion of thermocapillary forces in the analysis. Representative results for the flow and temperature distribution in the melt are shown graphically in the form of liquid phase isotherm and stream function distributions.

INTRODUCTION

SOLID–LIQUID phase change is a basic heat transfer phenomenon important in a variety of industrial applications. To date, considerable effort has been dedicated to solution of freezing and melting problems both in the absence of liquid phase convection and in situations where natural convection in the melt significantly affects freezing and melting [1, 2].

Under certain conditions, melt convection may be induced by driving forces in addition to buoyancy. For example, if the melt is characterized by a free surface, melt convection can be influenced by thermocapillary forces. Specifically, thermocapillary (Marangoni) convection plays a significant role in applications such as welding, crystal growth, and glass manufacturing [3–7]. The characteristics of these applications which promote the significance of Marangoni effects are relatively small geometries, high purity melts and free surface exposure to an inert environment. In larger geometries, buoyancy forces generally overshadow Marangoni effects while use of low purity materials in relatively active environments promotes species adsorption at the exposed surface. The surface species distribution adjusts to induce solutocapillary forces which offset their thermal counterparts resulting in effective no slip boundary conditions at this location [8].

Although considerable attention has been given to the effects of buoyancy in freezing and melting applications, as well as Marangoni effects in the absence of phase change, relatively little effort has been directed to the general case of combined buoyancy and Marangoni-induced melt convection with solid–liquid phase change. A combined numerical and experimental study involving a high Pr melt (n-octadecane) in a rectangular enclosure with heated and cooled side walls has been reported [9], and a numerical analysis of steady-state conjugate heat transfer in the same geometry has been considered [10]. Both studies have shown that thermocapillary convection can influence melting or solidification by enhancing or reducing solid–liquid interface heat transfer rates near the free surface and the bottom of the enclosure, respectively. In contrast, recent simulations of pure metal solidification at a vertical wall accounting for buoyancy forces only have not been in good agreement with experimental results, and the discrepancy has been attributed in part to uncertainties regarding the free surface hydrodynamic boundary conditions [11].

Perhaps the paucity of attention directed to Marangoni effects in freezing and melting is related to the difficulty in observing Marangoni phenomena in the heat transfer laboratory where a relatively dirty environment is present. However, in applications where the solid material purity demands are high, such as in microelectronics crystal growth, thermocapillary phenomena are observable and can be significant [12]. Hence, the objective of this study is to consider how Marangoni and buoyancy forces interact to influence

NOMENCLATURE

A cavity aspect ratio, H/W
c_l liquid specific heat
$F(Y,\tau)$ dimensionless solid–liquid interface position
Fo Fourier number, $\alpha t/H^2$
g gravitational acceleration
H liquid metal height
Δh_f latent heat of fusion
k thermal conductivity
Ma Marangoni number, $\sigma'(T_w-T_f)H/\mu\alpha$
Nu local Nusselt number, $qH/k(T_w-T_f)$
$\vec{n}$ unit vector normal to the solid–liquid interface
P dimensionless local pressure
$\tilde{P}$ reduced pressure in pressure and mass flux interpolations
Pr Prandtl number, ν/α
q local heat flux
Ra Rayleigh number, $g\beta(T_w-T_f)H^3/\nu\alpha$
Ste Stefan number, $c_l(T_w-T_f)/\Delta h_f$
t time
T temperature
u velocity in the x-direction
U dimensionless velocity, uH/α
v velocity in the y-direction
V dimensionless velocity, vH/α
V^* molten volume fraction
V_n dimensionless normal melt front velocity
w melt free surface length
x coordinate direction normal to heated wall
X dimensionless coordinate, x/H
y coordinate direction parallel to heated wall
Y dimensionless coordinate, y/H.

Greek symbols

α thermal diffusivity
β thermal expansion coefficient
θ dimensionless temperature, $(T-T_f)/(T_w-T_f)$
μ dynamic viscosity
ν kinematic viscosity
ρ^* density ratio, ρ_s/ρ_l
σ fluid surface tension
σ' surface tension variation with temperature, $\partial\sigma/\partial T$
τ dimensionless time, $Fo\ Ste$
ψ^* dimensional stream function
Ω length scale in $\tilde{P}$–Ω scheme.

Subscripts

f fusion point
i solid–liquid interface
l liquid quantity
w heated wall quantity
x x-direction quantity
y y-direction quantity.

a solid–liquid phase change process. Specifically, consideration is given to the physical system shown in Fig. 1. Here, a solid material is contained within an enclosure and is initially at its fusion temperature. The material is melted by impulsively heating the left enclosure wall above the fusion temperature. The material's top surface is either exposed to an inert environment so that both buoyancy and surface tension forces exert their full influence on the melt convection, or is characterized by effective no slip hydrodynamic boundary conditions. The physical situation which motivates the specification of the dimensionless parameters of the study is melting of a silicon ribbon with a thickness of approximately 5, 10, and 20 mm. Variations in the silicon thickness lead to changes in the relative influence of buoyancy and surface tension forces, as will become evident.

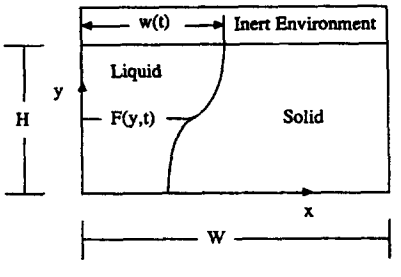

FIG. 1. Schematic of the physical system.

ANALYSIS

Two-dimensional melting of a solid slab of pure metal from an isothermal vertical wall is modeled mathematically. In general, the melt is characterized by a free liquid surface and undergoes convection due to the presence of buoyancy and thermocapillary forces. The metal is assumed to be initially at its fusion temperature T_f, eliminating the need for solution of the energy equation in the solid. At time $t = 0$ the temperature of one vertical wall of height H is raised impulsively to a prescribed temperature above the fusion point, $T_w > T_f$.

In order to simplify the analysis, certain assumptions consistent with recent numerical treatments of combined surface tension/buoyancy induced flow and melting processes have been made. The melt free surface is assumed to be flat and nondeformable. The Boussinesq approximation is employed and the surface tension is assumed to vary linearly with temperature. The thermophysical properties of the melt are evaluated at $(T_w+T_f)/2$ and the flow and heat transfer are assumed to be laminar. Viscous dis-

sipation is neglected, as are the slight normal velocities at the solid–liquid interface due to the material density change upon melting.

Due to the high melting temperature of most liquid metals, it may be anticipated that radiative exchange between the free surface and the environment above will redistribute surface temperatures and impact thermocapillary phenomena. A preliminary numerical investigation was performed in which a layer of molten silicon with $w/H = 2.0$ was held within a square enclosure. The vertical enclosure walls were maintained at T_w and T_f, while the ceiling and bottom of the enclosure were characterized by a linear temperature distribution and adiabatic thermal boundary conditions, respectively. Radiative exchange between differential areas located on the melt surface and diffuse gray enclosure walls was included in the simulation of thermocapillary flow within the melt. For a range of operating conditions similar to those considered here and for wall emissivities between 0.1 and 0.9, thermocapillary convection within the melt (with a conservatively estimated molten surface emissivity of 0.75) was, for all practical purposes, unaffected by radiative exchange. Local cold wall heat transfer rates were affected only marginally, with uniform shifts of approximately 10% over the range of wall emissivities considered. In light of these results, the horizontal bounding surfaces are considered to be adiabatic in this study.

Under the foregoing assumptions, the partial differential equations governing the transport of mass, momentum, and energy in dimensionless form are

continuity

$$\frac{\partial U}{\partial X} + \frac{\partial V}{\partial Y} = 0; \tag{1}$$

momentum

$$\frac{\partial U}{\partial Fo} + U\frac{\partial U}{\partial X} + V\frac{\partial U}{\partial Y} = -\frac{\partial P}{\partial X} + Pr\left(\frac{\partial^2 U}{\partial X^2} + \frac{\partial^2 U}{\partial Y^2}\right) \tag{2}$$

$$\frac{\partial V}{\partial Fo} + U\frac{\partial V}{\partial X} + V\frac{\partial V}{\partial Y} = -\frac{\partial P}{\partial Y} + Pr\left(\frac{\partial^2 V}{\partial X^2} + \frac{\partial^2 V}{\partial Y^2}\right) + Ra\,Pr\,\theta; \tag{3}$$

energy

$$\frac{\partial \theta}{\partial Fo} + U\frac{\partial \theta}{\partial X} + V\frac{\partial \theta}{\partial Y} = \frac{\partial^2 \theta}{\partial X^2} + \frac{\partial^2 \theta}{\partial Y^2}. \tag{4}$$

The boundary conditions applied to the melt are:

at heated wall, $X = 0$

$$U = V = 0$$

$$\theta = 1; \tag{5a}$$

at the solid–liquid interface, $X = F(Y, \tau)$

$$U = V = 0$$

$$\theta = 0; \tag{5b}$$

at the bottom of the melt, $Y = 0$

$$U = V = 0$$

$$\frac{\partial \theta}{\partial Y} = 0; \tag{5c}$$

at the melt free surface, $Y = 1$

$$V = 0$$

$$\frac{\partial U}{\partial Y} = Ma\frac{\partial \theta}{\partial X} \tag{5d}$$

or

$$U = 0$$

$$\frac{\partial \theta}{\partial Y} = 0.$$

It should be noted that the Marangoni number appearing in equation (5d) is a ratio of thermocapillary to viscous forces in the melt. Due to the limited choice of a normalizing length scale, the system height, H, was selected. As such, Ma used in this study is rather artificial since it is usually defined in terms of the free surface length, w. Since w is an outcome of the solution here, recourse to utilization of a more physically meaningful length scale in Ma is prohibited.

To complete the specification of the problem an energy balance is performed at the solid–liquid interface, yielding

$$-\nabla\theta\cdot\bar{\mathbf{n}} = \rho^*\frac{V_n}{Ste} \tag{6}$$

where $-\nabla\theta\cdot\bar{\mathbf{n}}$ is the local normal heat flux to the solid–liquid interface and V_n the dimensionless local normal interface velocity.

Numerous methodologies have been used to predict melting in the presence of natural convection [2, 13–16]. A control-volume based discretization scheme was employed in this study. The salient features of the solution method, which has been used previously to simulate buoyancy-only melting of pure metals [18] are the following. The governing partial differential equations in terms of primitive variables were integrated over discrete non-orthogonal control volumes in the melt domain. All terms arising from the non-orthogonality of the grid were retained in the solution procedure.The melt front was advanced by invoking the quasi-steady assumption; the melting process was assumed to take place via a series of steady-state periods during which the solid–liquid interface was immobilized. The computational procedure could then be divided into two parts: the steady-state advec-

tion–diffusion iterations, and the solid–liquid interface displacement.

The scheme used for the solution for the advection–diffusion equations is a modification of that presented in ref. [17] and discussed in ref. [18].The power-law formulation of Patankar [19] was employed and additional terms arising from the nonorthogonality of the grid are treated as sources in the discretized equations. The dependent variables, U, V, P and θ are stored at the same node and the $\tilde{P}$–Ω scheme [17] was employed to interpolate mass fluxes and pressures to the control surfaces in order to avoid the prediction of unrealistic velocity and pressure fields [19].

With the converged temperature field for each time step the local interface heat flux in equation (6) is evaluated. The solid–liquid interface energy balance is scanned over the entire interface, and the time step is then selected such that the maximum local interface displacement is less than 5% of the corresponding local melt gap width. This ensures that the time step is small early in the melting process, when heat transfer rates to the solid–liquid interface and hence interface velocities, are high. Later, after the establishment of quasi-steady melting, the time step increases. After the interface is displaced, the steady-state advection–diffusion equations are re-solved.

An algebraically generated non-orthogonal grid was used to define the control surfaces of the grid system. Horizontal and nominally vertical control surfaces were determined with power-law clustering schemes over half of the melt domain

$$Y_j = \frac{1}{2}\left(\frac{j-1}{M}\right)^m, \quad j = 1,2,\ldots,M+1 \tag{7}$$

$$X_i = \frac{F(Y,\tau)}{2}\left(\frac{i-1}{N}\right)^n, \quad i = 1,2,\ldots,N+1 \tag{8}$$

where $2M$ and $2N$ are the number of control volumes in the Y- and X-directions, respectively. The remaining half of the control surfaces were generated so that the grid distribution was symmetric about $Y = 1/2$ and $X = F(Y,\tau)/2$. The horizontal control surfaces were generated once and remained unchanged throughout the simulation. Generation of the vertical control surfaces was performed at each time step according to equation (8).

Considerable care and compromise is involved in the selection of m, n, M and N in this study, beyond that associated with the analysis of pure buoyancy melting. Ideally, the control surfaces will be deployed in a manner which leads to faithful prediction of local heat transfer rates at the solid–liquid interface, melt convection in the far field, and secondary recirculations. For the pure buoyancy case, a nearly uniform distribution ($m = 1.25$) for the horizontal control surfaces and clustering of nodes near the heated vertical wall and melt front ($n = 1.75$), used in conjunction with a relatively coarse grid (20×24 control volumes) has been reported previously [18]. This grid distribution was selected as a compromise between computational cost considerations and attainment of grid-independent results.

In contrast to the comparatively modest grid spacing requirements for low Rayleigh number, pure buoyancy simulations, numerical simulations of pure thermocapillary-induced convection can demand utilization of very fine grid networks. For example, in the case of pure thermocapillary-induced flow in a square enclosure with a $Pr = 1$ fluid, extremely fine grid networks (approximately 150 control volumes in both X and Y) are necessary to resolve details of the flow and even finer networks may be necessary for liquid metals [20]. These severe mesh refinements are necessary due to isotherm compaction resulting from Marangoni convection-intensified flow at the top of the cold wall. The steep temperature gradients induce increased surface velocities through the free surface hydrodynamic boundary condition (equation (5d)) which, in turn, promote steep temperature gradients, etc. The resulting thermocapillary forces can become so large that maximum surface velocities can be predicted (unrealistically) at the grid node adjacent to the cold wall.

Noting the reported expense of pure buoyancy melting simulations [18] it is impractical to incorporate extremely fine grids in solid–liquid phase change problems with significant thermocapillary effects included in the analysis. Fortunately, however, the consequences of using a relatively coarse grid are not as serious in the melting problem as implied by the previous discussion. When the thermocapillary forces are included in the liquid phase, isotherm compaction at the top of the cold wall leads to relatively large local heat transfer rates at this location [21]. As a result, 'notching' of the solid will occur and a thin, nearly-horizontal finger of liquid will extend above the solid [22]. Within the notch, the melt must negotiate a sharp (nearly 180°) turn in order to return to the bulk of the liquid phase. As a result, the free surface velocities are slower relative to the enclosure problem, since the underlying fluid is traveling away from the cold wall. Viscous damping of thermocapillary-induced flow due to solid notching has been noted previously in conjugate solid–liquid simulations including buoyancy and thermocapillary effects and the grid size restrictions may be relaxed considerably in order to achieve grid independent results [10].

In this study, values of m, n, M and N are 1.10, 1.75, 15 and 12 (30×24 control volumes), respectively. The selected values are a compromise between achievement of problem tractability and resolution of the details of the flow field. In defense of the grid generation scheme, none of the simulations reported here are characterized by maximum free surface velocities immediately adjacent to the solid–liquid interface.

The calculation procedure was initialized with a thin layer thickness at a dimensionless time given by the conduction solution. The initial time was $Fo = 1$, and the corresponding Rayleigh number based on gap width was always less than 250. The solution for the

flow field at each quasi-steady time step proceeded until the heat transfer rates at the hot wall and the solid–liquid interface agreed to within 0.001%. In general, the corresponding maximum mass residual within the melt was of the order of 10^{-7}.

RESULTS

The physical system associated with the simulations is the melting of a pure silicon layer of various heights. The solid silicon is initially at its fusion temperature and the left wall of the enclosure is raised impulsively to 10°C above T_f. No slip and Marangoni hydrodynamic boundary conditions, respectively, are applied at $Y = 1$ in order to consider the limiting surface tension effects. The thermophysical properties of silicon are from refs. [23–25].

The Stefan and Prandtl numbers associated with the simulations are 0.005 and 0.03, respectively. Simulations were made for $Ra = 4.0 \times 10^2$, 3.0×10^3 and 2.5×10^4 and $Ma = 1.0 \times 10^3$, 2.0×10^3 and 4.0×10^3. These dimensionless parameters correspond to silicon ribbon heights of 5, 10 and 20 mm, respectively. The silicon layer heights were selected in order to consider a range of conditions where either buoyancy or thermocapillary effects dominate the melting process. The ratio of buoyancy to surface tension forces is described by the dynamic Bond number, $Bo = Ra/Ma$. The simulations are characterized by $Bo = 0.40$, 1.50 and 6.25, suggesting that the impact of thermocapillary phenomena diminishes as the silicon height is increased. The dimensionless stream function is evaluated in order to ascertain the strength of the convective motion and is defined in the usual way

$$U = \frac{\partial \psi}{\partial Y}, \quad V = -\frac{\partial \psi}{\partial X} \tag{9}$$

where the stream function at $X = 0$, $Y = 0$ has been arbitrarily taken to be zero. The dimensionless stream function ψ may be expressed in terms of the dimensional stream function as $\psi = \psi^* Pr/\nu$.

The results of Fig. 2 are associated with the imposition of no-slip boundary conditions for the thickest silicon layer, $H = 20$ mm, and are consistent with those previously reported for melting liquid metals including only natural convection effects [18]. These results serve as a benchmark with which thermocapillary-assisted melting may be compared. Advection of relatively warm fluid from the hot left wall to the solid–liquid interface induces accelerated melting near the top of the phase change boundary. Weak recirculations are predicted to occur within the melt at intermediate (Fig. 2(b)) and later (Fig. 2(c)) times.

Relative to the previous discussions concerning the effect of surface contamination, the results of Fig. 2 correspond to melting of liquid metals with an adsorbed film layer or slag providing effective no slip hydrodynamic boundary conditions. In the absence of contamination, thermal surface tension forces will exert their full influence on the melt and will assist buoyancy effects in driving melt convection. Representative results for the same melting scenario associated with Fig. 2, but including surface tension effects are shown in Fig. 3.

Differences between Figs. 2 and 3 are readily apparent. As expected, inclusion of surface tension forces in the analysis induces relatively large melt velocities at the free surface. Due to the absence of no slip conditions at $Y = 1$, the center of rotation of the main cell is raised, relative to its position for the pure buoyancy simulation. The magnitudes of the maximum dimensionless surface velocities are 350, 225 and 185 for Figs. 3(a)–(c), respectively, and reflect the reduction in the average horizontal surface temperature gradient with increasing melt gap width at the free surface. Because of the increased melt velocities at the free surface, thermal advection from the warm left wall to the solid–liquid interface is enhanced. Accordingly, isotherm compaction is amplified at $Y = 1$, $X = F(Y, \tau)$, melting rates are increased near the free surface, and notching of the solid results.

As the fluid cools near the phase change interface it drops into the bulk of the melt and is no longer directly influenced by surface tension forces. The fluid parcels are sent down the chute-like profile of the solid–liquid interface and are returned to the hot wall. As a result of this flow, a weak recirculation is induced below the lip of the chute in much the same manner as observed in Fig. 2. In contrast with previous results, the recirculation evident at $X = 0$, $Y = 1$ in Fig. 2 disappears as thermocapillary forces assist their buoyancy counterparts and lead to well-behaved flow at this location.

Figures 4 and 5 include the local cold and hot wall Nusselt number, respectively, at various times for the simulations of Figs. 2 and 3. As is evident, overall heat transfer rates across the melt layer decrease with time as the molten material poses an ever-increasing thermal resistance between the warm wall and the solid–liquid interface. Variations in the local Nu may be traced to the combined effects of buoyancy and thermocapillary forces and the shape of the solid–liquid interface.

As seen in Fig. 4(a), which is associated with the imposition of no slip conditions at $Y = 1$, natural convection induces enhanced melting at the solid–liquid interface in the upper portions of the domain. Local heat transfer rates, for example in the vicinity of $Y = 0.3$, may increase with time and this seemingly anomalous behavior is traced to temporal variations in the solid–liquid interface shape.

Inspection of Fig. 4(b), which is associated with combined thermocapillary and buoyancy induced flow, reveals the increased local heat transfer resulting from isotherm compaction at the top of the solid–liquid interface. Whereas the spatial variations of Nu are relatively smooth in Fig. 4(a), sharper variations occur as thermocapillary effects are included in the analysis. Particularly noteworthy are the 'S' shaped

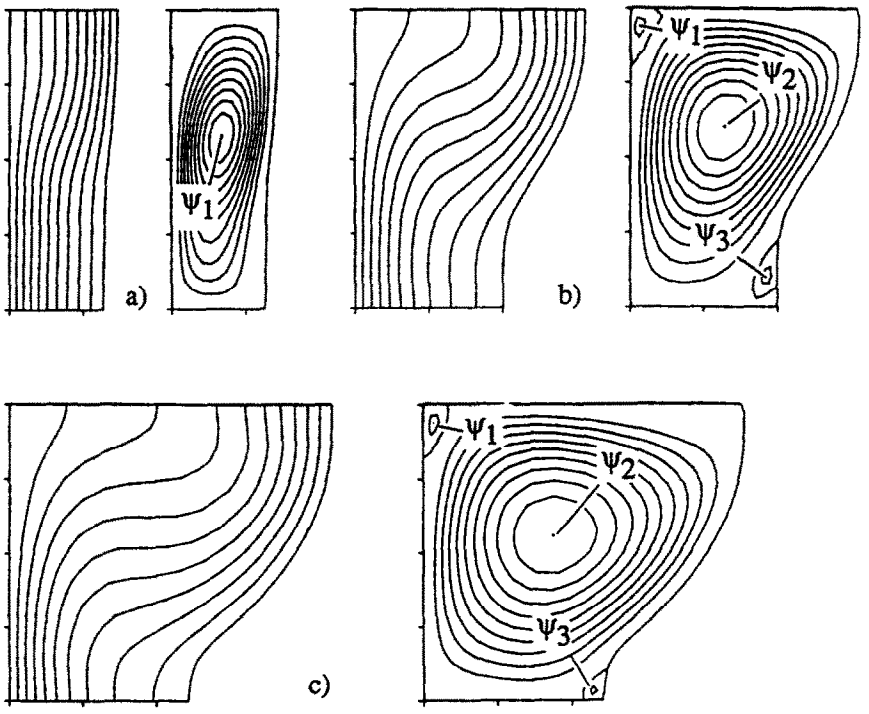

FIG. 2. Predicted melt streamlines and isotherms for $Ra = 2.5 \times 10^4$ and no slip boundary conditions: (a) $\tau = 0.05$, $\psi_1 = -1.9$; (b) $\tau = 0.15$, $\psi_1 = 0.04$, $\psi_2 = -3.5$, $\psi_3 = 0.01$; (c) $\tau = 0.25$, $\psi_1 = 0.04$, $\psi_2 = -4.2$, $\psi_3 = 0.01$.

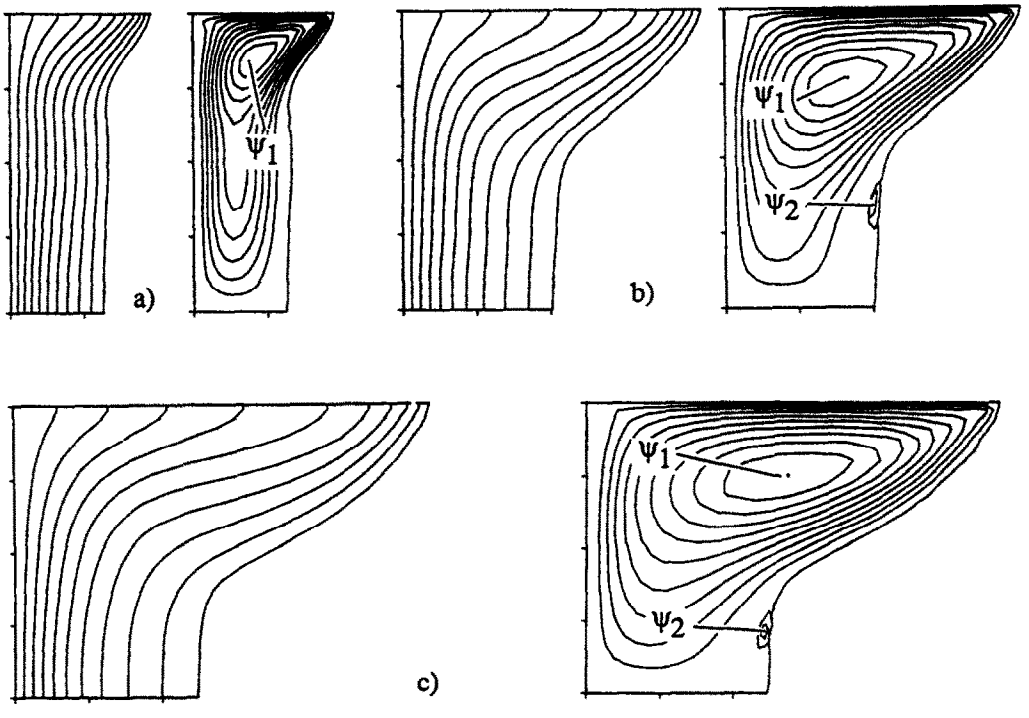

FIG. 3. Predicted melt streamlines and isotherms for $Ra = 2.5 \times 10^4$ and $Ma = 4 \times 10^3$: (a) $\tau = 0.05$, $\psi_1 = -2.3$; (b) $\tau = 0.15$, $\psi_1 = -3.6$, $\psi_2 = 0.004$; (c) $\tau = 0.25$, $\psi_1 = -4.2$, $\psi_2 = 0.003$.

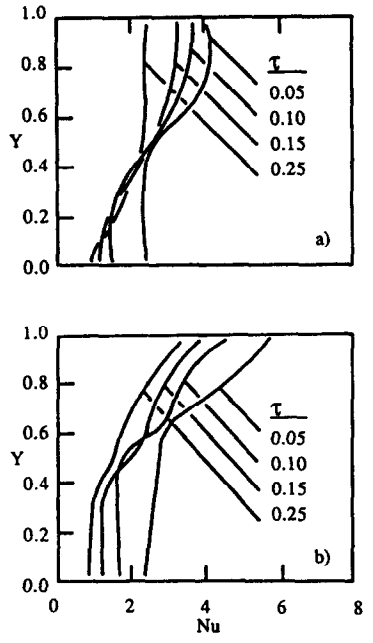

FIG. 4. Predicted interface *Nu* for the results of (a) Fig. 2 and (b) Fig. 3.

spatial variations in *Nu* at, for example, $Y \approx 0.6$ for $\tau = 0.10$. Within the 'S' distribution, relatively low local heat transfer rates are associated with the recirculation beneath the lip of the liquid–solid interface chute. Relatively high heat transfer occurs above the recirculation and is responsible for the propagation of notching to eventually include most of the *Y* range.

Warm wall Nusselt number distributions associated with the simulations of Figs. 2 and 3 are shown in Figs. 5(a) and (b), respectively. In general, the *Nu* distributions at the warm wall are of little interest, but reflect the modifications in the system hydrodynamics induced by thermocapillary phenomena.

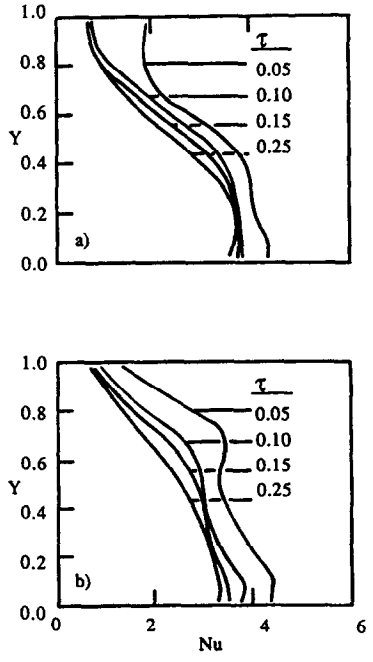

FIG. 5. Predicted hot wall *Nu* for the results of (a) Fig. 2 and (b) Fig. 3.

As was seen in Fig. 4, overall heat transfer rates across the melt decrease with time. However, the local Nusselt number at the hot wall decreases everywhere due to the planar system boundary. As expected, the inclusion of thermocapillary forces in the analysis decreases *Nu* near the upper surface of the warm wall due to destruction of the recirculation which occurs near this location when no slip boundary conditions are applied. Local curvature in the *Nu* distribution is more pronounced when surface tension effects are included and is traceable to the relatively active flow in the upper portions of the melt.

As *Bo* decreases with decreasing *H*, transition to thermocapillary-dominated flow is expected to occur. The results of Fig. 6 are associated with the smallest *H*, *Ra*, *Ma* and *Bo* (5 mm, 400, 1000 and 0.4, respectively). The predictions for the no slip case are not presented since the system response is conduction dominated and the solid–liquid interface is vertical.

For Marangoni-dominated conditions, complex multicellular convection is predicted to occur throughout the duration of the simulation. At early times ($\tau = 0.05$, Fig. 6(a)), a series of stacked convection cells occupies the melt region. The uppermost cell is most vigorous and is driven by thermocapillary forces at $Y = 1$. The thermocapillary effects propagate throughout the bulk of the melt and the middle cell rotates in a counter-clockwise fashion in defiance of the buoyancy forces within the system. In turn, the bottom-most cell is rotated by viscous forces exerted at its interface with the middle cell, as well as the buoyancy forces within the system.

The uppermost convection cell is of sufficient strength to promote significant advection within the melt. Advective action compacts isotherms at the top of the solid–liquid interface and leads to interface notching. In contrast, the vertical, uniformly-spaced isotherms in the lower two-thirds of the melt suggest conduction-dominated transport.

As time progresses, the two secondary cells shift their relative positions and, eventually, the middle cell retreats to a position beneath the lip of the solid–liquid interface chute at $\tau = 0.25$ (Fig. 6(c)). As noted for the higher *Bo* results of Fig. 3, the maximum dimensionless melt surface velocities continually decrease as the melt thickness increases and are 72, 50 and 42 for $\tau = 0.05$, 0.15 and 0.25, respectively.

Figure 7 presents interface and hot wall local Nusselt number distributions associated with the results of Fig. 6. Inspection of Fig. 7(a) reveals the decrease in the overall *Nu* as the melt width increases. Thermocapillary forces induce the high melting rates near the free surface and their effects penetrate further downward as the melt width increases. The 'S' shaped *Nu* distributions are more distinct than those of Fig. 4(b) and are again attributed to the solid–liquid inter-

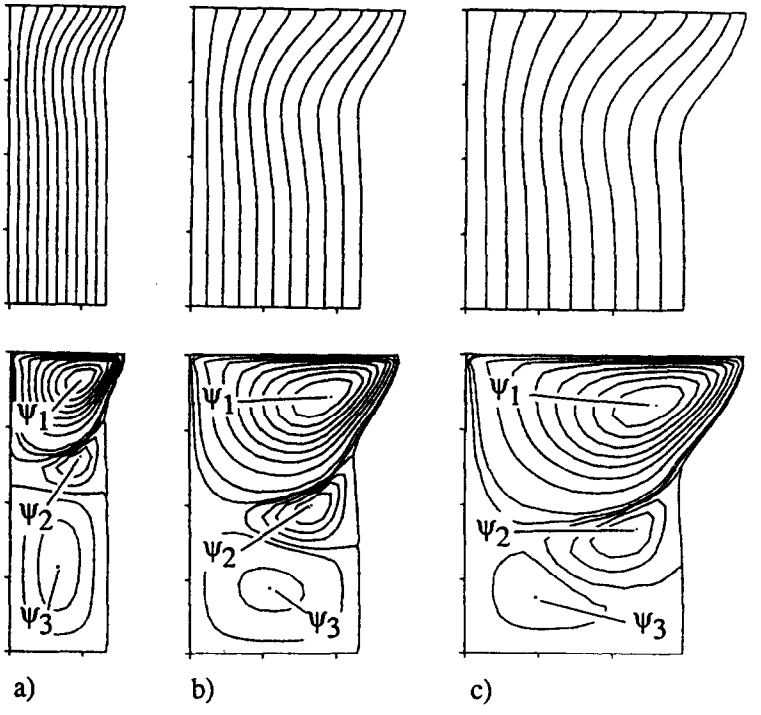

FIG. 6. Predicted melt streamlines and isotherms for $Ra = 400$ and $Ma = 1 \times 10^3$: (a) $\tau = 0.05$, $\psi_1 = -1.0$, $\psi_2 = 0.025$, $\psi_3 = -0.038$; (b) $\tau = 0.15$, $\psi_1 = -1.3$, $\psi_2 = 0.045$, $\psi_3 = -0.05$; (c) $\tau = 0.25$, $\psi_1 = -1.4$, $\psi_2 = 0.051$, $\psi_3 = -0.026$.

face shape and the presence of the secondary recirculation. In the bottom half of the system, however, existence of conduction-dominated heat transfer is suggested.

The warm wall *Nu* distributions of Fig. 7(b) also reflect the influence of thermocapillarity at $Y = 1$ with small *Nu* existing at this location. Although the uniform *Nu* distributions at small *Y* seem to indicate conduction-dominated conditions, a comparison of hot and cold wall *Nu* values shows that advective thermal transport is important, even in the lower portions of the melt region. Indeed, a difference in hot and cold wall *Nu* values is required in order to offset the variations in *Nu* at large *Y* and conserve energy on a global basis.

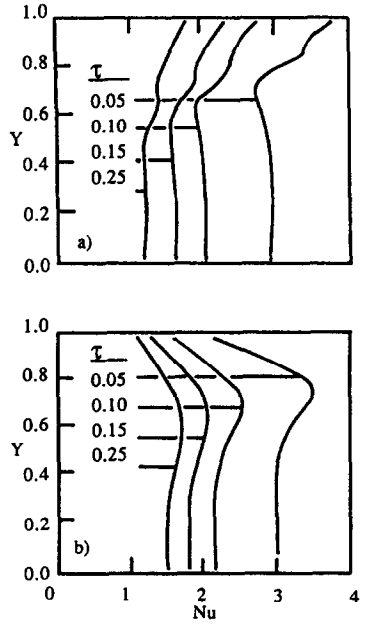

FIG. 7. Predicted (a) interface *Nu* and (b) hot wall *Nu* for the results of Fig. 6.

As is evident in the results thus far, variations in the convective transport within the melt due to inclusion of surface tension forces in the analysis lead to changes in the local melting rates at the solid–liquid interface. A summary of the resulting modifications to the timewise variation of the solid–liquid interface location, at various times, is shown in Fig. 8.

As the height of the silicon layer is increased, both buoyancy and thermocapillary forces are enhanced and accelerated melting occurs. Locally, however, the width of the melt region may actually decrease when Marangoni effects are taken into account. For all of the cases considered here, a thicker melt region at $Y = 1$ coincides with a thinner melt region at the *Y* location of the secondary recirculation noted in the previous figures. In general, the melt widths for the Marangoni and no slip simulations coincide at small *Y*.

Although significant variations in the local melt width are induced by thermocapillary effects, the complex interactions between the melt and the solid lead

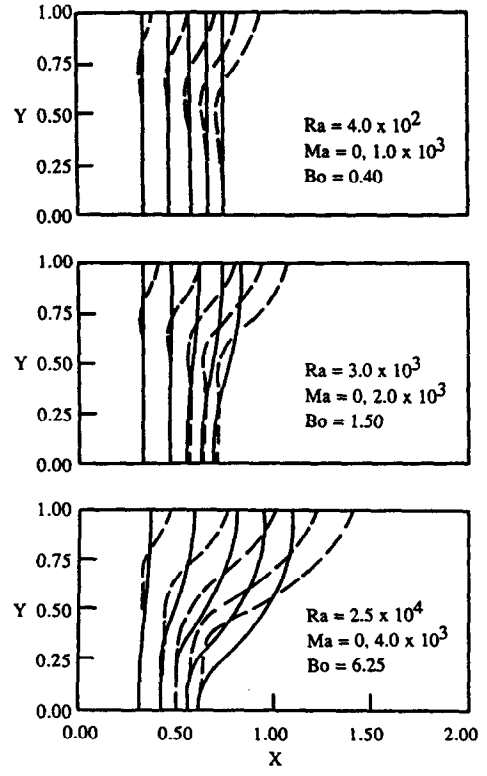

FIG. 8. Predicted solid–liquid interface positions at various times. The interface positions correspond to imposition of no slip (solid line) and Marangoni (dashed line) hydrodynamic boundary conditions. The interface locations are shown at $\tau = 0.1$, 0.2, 0.3, 0.4 and 0.5, from left to right.

to less severe variations in the overall melting rate. To quantify this notion, the molten fraction may be obtained from a numerical integration of the melt cavity volume

$$V^* = A \int_0^1 F(Y, \tau)\, dY \qquad (10)$$

where the aspect ratio for all the simulations is 0.5. The dimensionless melt volume for all of the simulations is plotted vs time in Fig. 9.

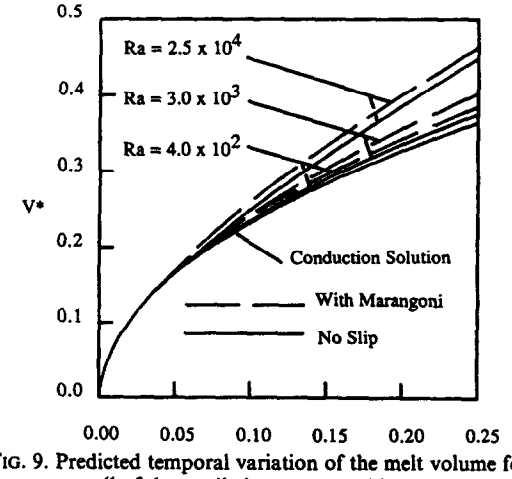

FIG. 9. Predicted temporal variation of the melt volume for all of the predictions presented here.

The results of Fig. 9 indicate that the melt volume increases as convective effects (Ra) are increased within the system. Surprisingly, however, the nature of the hydrodynamic boundary condition imposed at $Y = 1$ wields little influence on the overall melting rate. For example, at $Ra = 2.5 \times 10^4$, inclusion of thermocapillary effects is responsible for only a 3% increase in the melt fraction at $\tau = 0.25$. In contrast, thermocapillary effects are responsible for variations in the local melt thickness of approximately 30% at the same time for the same simulation. Again, the disparity in the importance of thermocapillary effects is attributed to local increases and decreases in melting rates at the phase change interface due to the complex hydrodynamic flow field interaction with the solid.

CONCLUSIONS

Numerical predictions have been made for melting of a pure metal with combined buoyancy and surface tension forces included in the melt. Thermocapillary forces are observed to have a significant impact on the local melting behavior and shape of the solid–liquid interface. Isotherm compaction near the top of the melting front causes significantly higher local melting at this location relative to the pure buoyancy case. Complex multicellular flow patterns are observed in the melt, and this flow structure is intimately related to the local Nusselt number distribution, and hence, local melting rates along the solid–liquid interface. Whereas the influence of Marangoni convection is felt strongly by the local melting at the melt front, causing notching near the free surface, the resultant global melting rates are only marginally higher. As expected, surface tension effects diminish as the cavity height is increased.

Acknowledgements—One of the authors (T.L.B.) acknowledges support of this work by the National Science Foundation under Grant No. CBT-8552806. Computational facilities were made available by the Department of Mechanical Engineering, The University of Texas at Austin.

REFERENCES

1. M. N. Ozisik, *Heat Conduction*. Wiley-Interscience, New York (1980).
2. E. M. Sparrow, S. V. Patankar and S. Ramadhyani, Analysis of melting in the presence of natural convection in the melt region, *J. Heat Transfer* **99**, 520–526 (1977).
3. W. H. Giedt, Welding—an interdisciplinary science and technology. In *Interdisciplinary Issues in Materials Processing Manufacturing* (Edited by S. K. Samanta, R. Komanduri, R. McMeeking, M. M. Chen and A. Tseng), p. 403. ASME, New York (1987).
4. P. S. Wei and W. H. Giedt, Surface tension gradient-driven flow around an electron beam welding cavity, *Weld. J.* **64**, 251–259 (1985).
5. D. Schwabe and A. Scharmann, Thermocapillary convection in crystal growth melts, *Lett. Heat Mass Transfer* **7**, 282–293 (1980).
6. N. Kobayashi, Computer simulation of the steady flow

in a cylindrical floating zone under low gravity, *J. Crystal Growth* **66**, 63–72 (1984).
7. T. J. McNeil, R. Cole and R. S. Subramanian, Surface-tension-derived flow in a glass melt, *J. Am. Ceram. Soc.* **68**, 254–259 (1985).
8. R. Clift, J. R. Grace and M. E. Weber, *Bubbles, Drops and Particles*, p. 38. Academic Press, New York (1978).
9. T. Munakata and I. Tanasawa, Buoyancy and surface tension driven natural convection with solidification. In *Proc. Eighth Int. Heat Transfer Conf.* (Edited by C. L. Tien, V. P. Carey and J. K. Ferrell). Hemisphere, Washington, DC (1986).
10. J. R. Keller and T. L. Bergman, Prediction of steady-state convection in a solid/liquid system: inclusion of buoyancy and surface tension forces in the liquid phase, *Proc. 1988 Nat. Heat Transfer Conf.*, Vol. 3, pp. 101–108. ASME, New York (1988).
11. F. Wolff and R. Viskanta, Solidification of a pure metal at a vertical wall in the presence of liquid superheat, *Int. J. Heat Mass Transfer* **31**, 1735–1744 (1988).
12. D. Schwabe, Marangoni effects in crystal growth melts, *PhysicoChem. Hydrodynam.* **2**, 263–280 (1981).
13. C. J. Ho and R. Viskanta, Heat transfer during melting from an isothermal vertical wall, *J. Heat Transfer* **106**, 12–19 (1984).
14. A. Gadgil and D. Gobin, Analysis of two dimensional melting in rectangular enclosures in the presence of convection, *J. Heat Transfer* **106**, 20–26 (1984).
15. M. Okada, Analysis of heat transfer during melting from a vertical wall, *Int. J. Heat Mass Transfer* **27**, 2057–2066 (1984).
16. C. Benard, D. Gobin and F. Martinez, Melting in rectangular enclosures: experiments and numerical simulations, *J. Heat Transfer* **107**, 794–803 (1985).
17. C. F. Hsu, A curvilinear-coordinate method for momentum, heat and mass transfer in domains of irregular geometry, Ph.D. thesis, University of Minnesota, Minneapolis (1982).
18. B. W. Webb and R. Viskanta, Analysis of heat transfer during melting of a pure metal from an isothermal vertical wall, *Numer. Heat Transfer* **9**, 539–558 (1986).
19. S. V. Patankar, *Numerical Heat Transfer and Fluid Flow*. Hemisphere, Washington, DC (1980).
20. R. L. Zehr, M. M. Chen and J. Mazumder, Thermocapillary convection of a differentially heated cavity at high Marangoni numbers, ASME paper 87-HT-29, presented at the National Heat Transfer Conference, Pittsburgh, Pennsylvania (1987).
21. T. L. Bergman and S. Ramadhyani, Combined buoyancy, thermocapillary driven convection in open square cavities, *Numer. Heat. Transfer* **9**, 444–451 (1986).
22. V. Stanek and J. Szekely, The effect of surface driven flows on the dissolution of a partially immersed solid in a liquid—analysis, *Chem. Engng Sci.* **25**, 699–715 (1970).
23. D. Schwabe, A. Scharmann, F. Preisser and R. Oeder, Experiments on surface tension driven flow in floating zone melting, *J. Crystal Growth* **43**, 305–312 (1978).
24. S. Z. Beer, *Liquid Metals*. Marcel Decker, New York (1972).
25. S. C. Hardy, The surface tension of liquid silicon, *J. Crystal Growth* **69**, 456–460 (1984).

SIMULATION DE LA FUSION D'UN METAL PUR AVEC FORCE DE FLOTTEMENT ET TENSION SUPERFICIELLE DANS LA PHASE LIQUIDE

Résumé—On présente des résultats analytiques pour la fusion d'un métal pur à partir d'une paroi verticale isotherme. On dégage l'influence de la tension superficielle sur l'écoulement et le transfert thermique dans la phase liquide aussi bien qie la forme résultante et le mouvement de l'interface solide–liquide. Les prédictions numériques révèlent une interaction complexe entre les forces de flottement dans le bain et les effets de Marangoni à la surface libre. La convection pilotée par la tension interfaciale cause une compaction isotherme près du sommet adjacent du front de fusion. Le transfert thermique associé, à l'intersection de l'interface solide–liquide et de la surface libre est élevé et il résulte d'une "entaille" dans le solide. L'influence de la convection de Marangoni est trouvée dans la forme et le mouvement de l'interface solide–liquide. Les vitesses de fusion calculées montrent une faible sensibilité à l'introduction dans l'analyse des forces thermocapillaires. Des résultats représentatifs pour le champ de vitesse et la distribution de température dans le bain sont montrés graphiquement pour la forme de la phase liquide, les courbes d'isothermes et de fonction de courant.

SIMULATION DES SCHMELZENS VON REINEM METALL UNTER BERÜCKSICHTIGUNG VON AUFTRIEB UND OBERFLÄCHENSPANNUNG IN DER FLÜSSIGEN PHASE

Zusammenfassung—Es werden analytische Lösungen für das Schmelzen von reinem Metall einer isothermen senkrechten Wand vorgestellt. Die Untersuchungen beleuchten sowohl den Einfluß der Oberflächenspannung auf die Strömung und den Wärmetransport als auch die daraus resultierende Form und Bewegung der Grenzfläche zwischen Feststoff und Flüssigkeit. Es wird ein auf Kontrollvolumina basierendes Diskretisierungsverfahren angewandt, um die partiellen Differentialgleichungen im ungleichförmigen Schmelzbereich zu lösen, während die sich eigentlich bewegende Grenze durch die Annahme quasi-stationärer Bedingungen als stillstehend angesehen wird. Numerische Berechnungen lassen eine komplizierte Wechselwirkung zwischen Auftriebskräften in der Schmelze und den Marangoni-Effekten an deren freier Oberfläche erkennen. Die von der Oberflächenspannung angetriebene Konvektion verursacht im oberen Bereich der Schmelzfläche eine isotherme Verdichtung. Aus der damit verbundenen großen Wärmestromdichte an der Grenzfläche zwischen Feststoff und Flüssigkeit und an der freien Oberfläche der Schmelze resultiert eine bedeutende "Einkerbung" in der festen Phase. Daher macht sich der Einfluß der Marangoni-Konvektion bei der zeitlich veränderlichen Form und Bewegung der Grenzfläche stark bemerkbar. Die berechnete Gesamtschmelzgeschwindigkeit reagiert weniger empfindlich auf die Einbeziehung thermokapillarer Kräfte. Repräsentative Ergebnisse für das Strömungsfeld und die Temperaturverteilung in der Schmelze werden grafisch in der Form von Isothermen in der flüssigen Phase und in Stromfunktionsverteilungen gezeigt.

МОДЕЛИРОВАНИЕ ПЛАВЛЕНИЯ ЧИСТОГО МЕТАЛЛА С УЧЕТОМ ПОДЪЕМНОЙ СИЛЫ И СИЛЫ ПОВЕРХНОСТНОГО НАТЯЖЕНИЯ В ЖИДКОЙ ФАЗЕ

Аннотация—Представлены аналитические результаты для плавления чистого металла у изотермической вертикальной стенки. Исследуется влияние поверхностного натяжения на течение и теплоперенос в жидкой фазе, а также на результирующую форму и движение границы раздела между твердым веществом и жидкостью. Определяющие дифференциальные уравнения в частных производных в области плавления неправильной формы решаются на основе схемы объемной дискретизации, а движущаяся граница считается неподвижной в соответствии с допущением о квазистационарости. Численные расчеты показывают сложную связь между подъемными силами в расплаве и эффектами Марангони у свободной поверхности расплава. Конвекция, обусловленная поверхностным натяжением, вызывает изотермическое уплотнение над фронтом расплава и в прилегающей к нему области. Связанный теплоперенос на границе раздела между твердой и жидкой фазами, а также на свободной границе расплава приводит к заметному "зазубриванию" твердого вещества. Поэтому конвекция Марангони значительно влияет на зависящую от времени форму и движение границы между твердым телом и жидкостью. Однако рассчитанные скорости плавления металла в целом менее чувствительны к учету термокапиллярных сил. Характерные результаты для поля течения и распределения температур в расплаве показаны графически в форме изотермы жидкой фазы и линий тока.